Supplementary Information

Benchmarking Nanoparticulate Metal Oxide Electrocatalysts for the Alkaline Water Oxidation Reaction

Suho Jung, [*a] *Charles C. L. McCrory,* [*a] *Ivonne M. Ferrer,* [ab] *Jonas C. Peters,* [*ab] *and Thomas F. Jaramillo* [*ac]

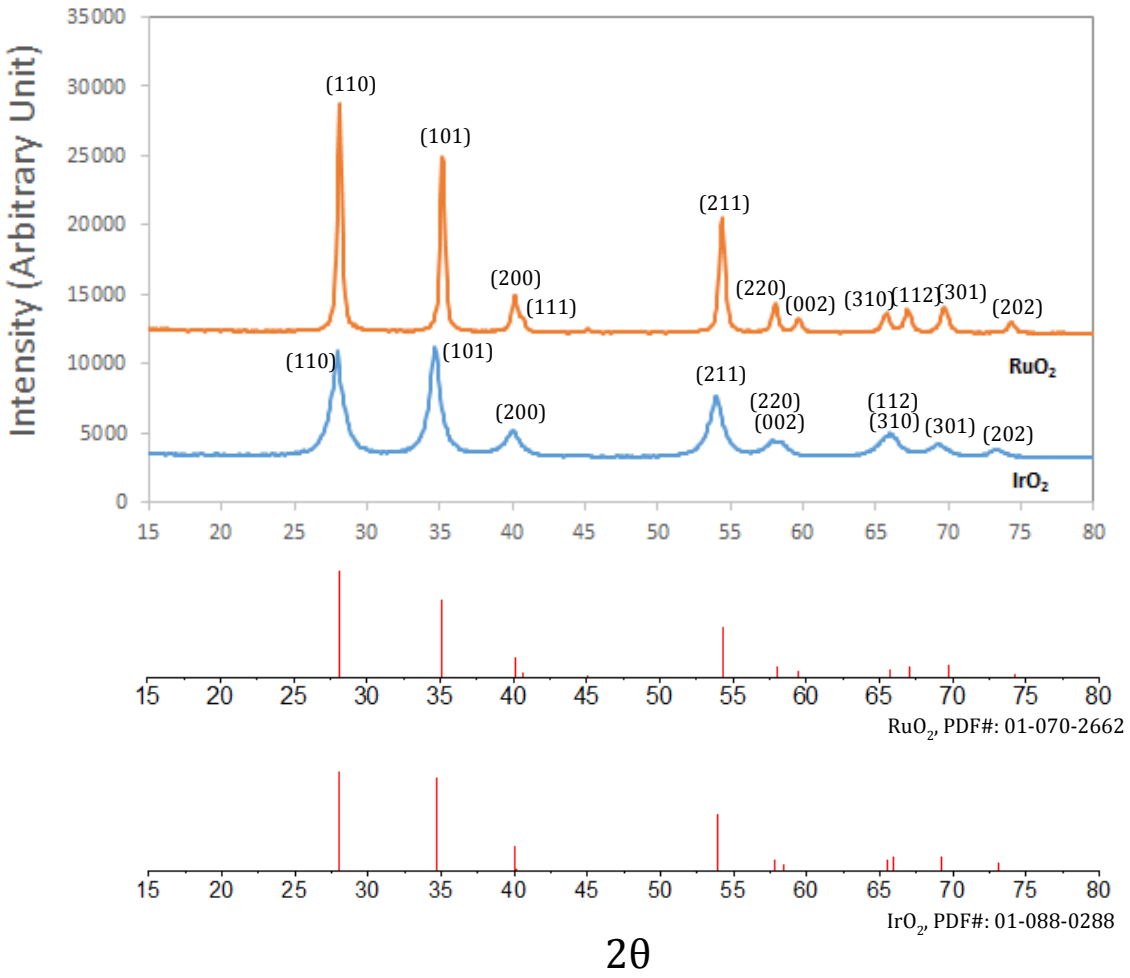

Figure S1. XRD patterns for noble metal oxides in rutile crystal structures. The broader peaks for IrO_2-(i) indicate a small particulate size. Reference patterns from ICDD are also shown below for matching and comparison.

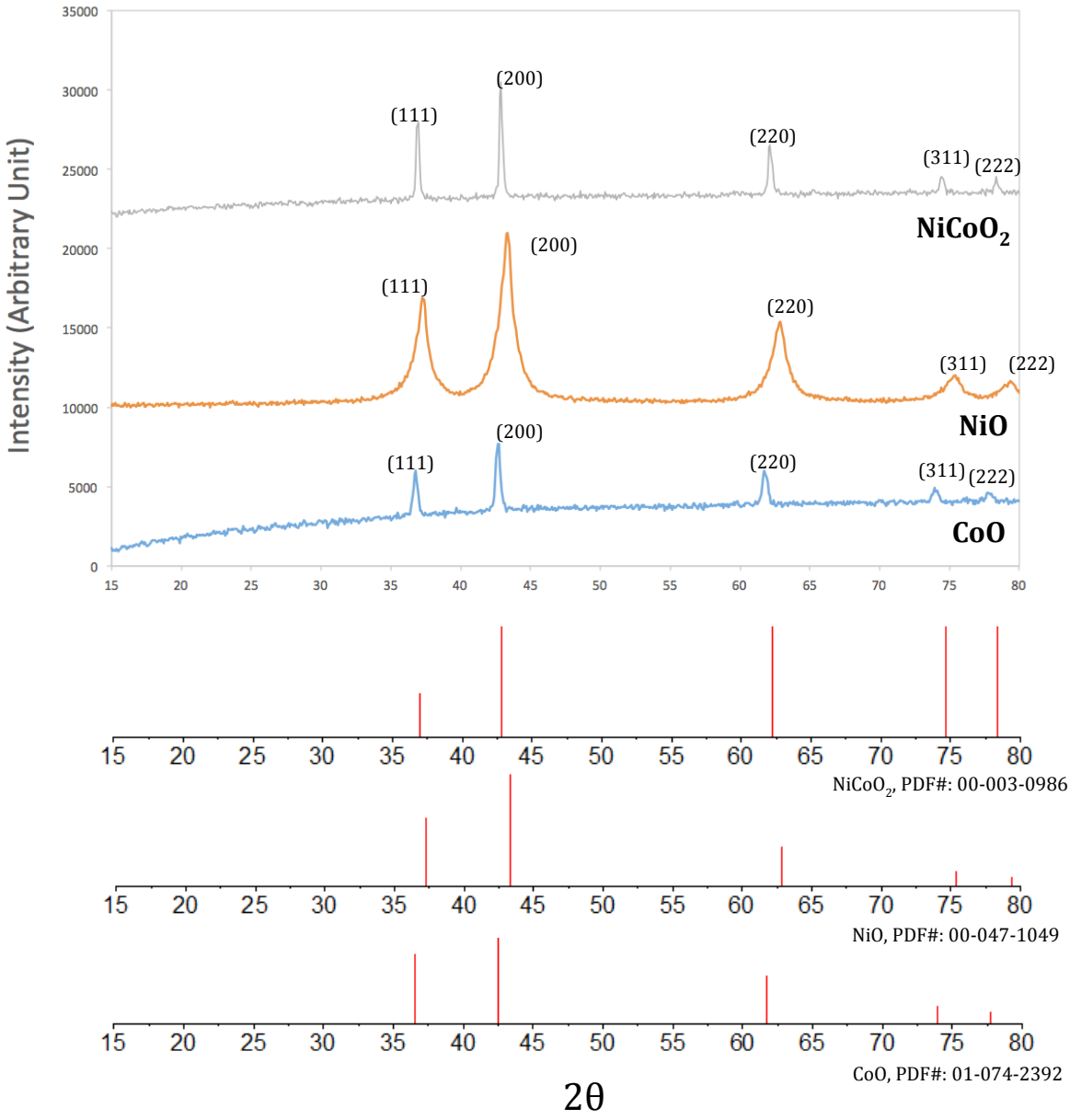

Figure S2. XRD patterns for first-row transition metal oxides in rock salt crystal structures. The broader peaks of NiO-(i) indicate a small particulate size. Reference patterns from ICDD are also shown below for matching and comparison.

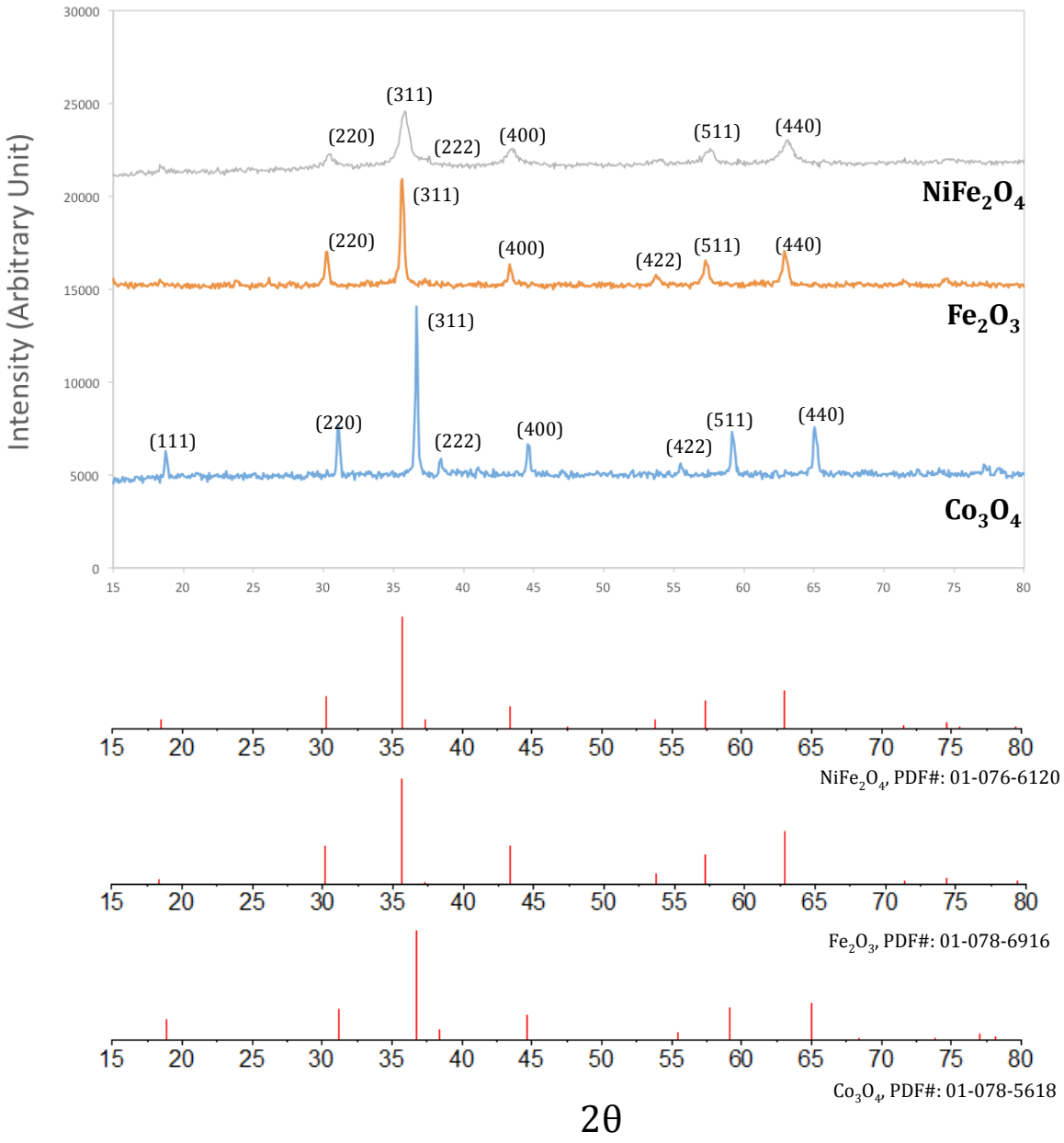

Figure S3. XRD patterns for first-row transition metal oxides in spinel crystal structures. The broader peaks of $NiFe_2O_4$ indicate a small particulate size. Reference patterns from ICDD are also shown below for matching and comparison.

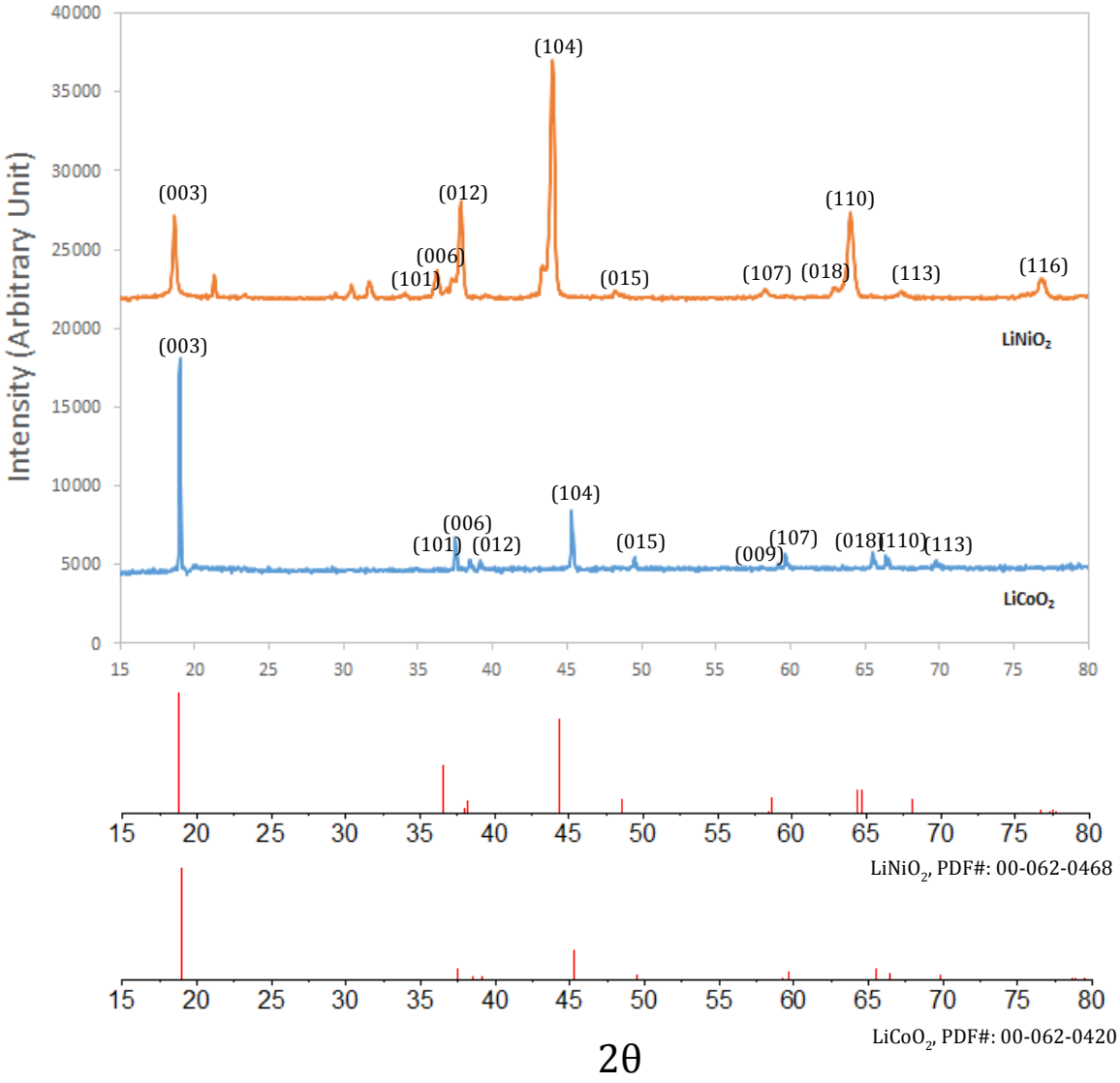

Figure S4. XRD patterns for Li-based layered rhombohedral oxides. There are some peaks not identified in the 2θ range of 20-35° for $LiNiO_2$, which may be attributed to an incomplete calcination from the supplier. Reference patterns from ICDD are also shown below for matching and comparison.

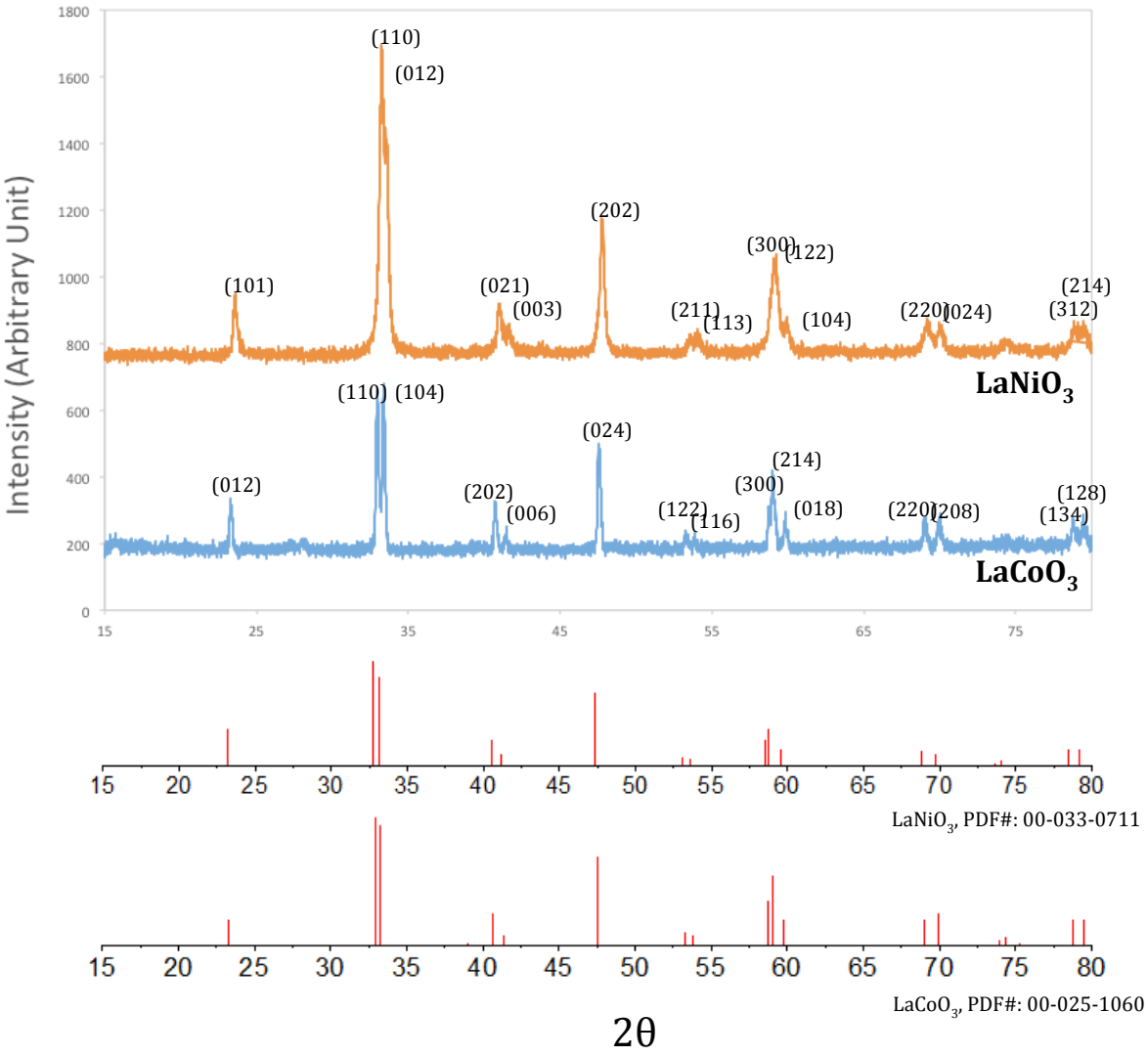

Figure S5. XRD patterns for La-based perovskite oxides. These two perovskites were synthesized in the laboratory. Reference patterns from ICDD are also shown below for matching and comparison.

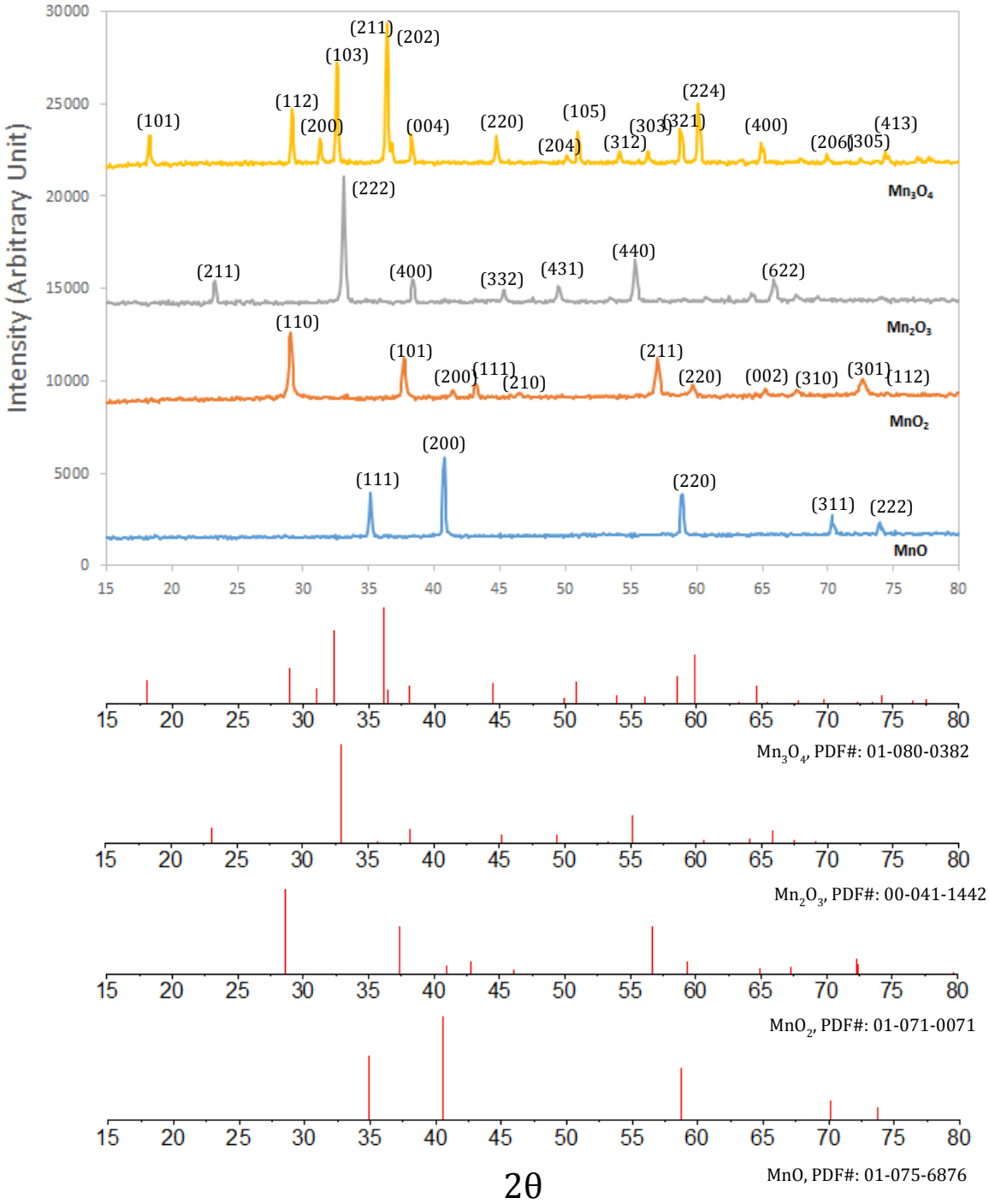

Figure S6. XRD patterns for various manganese oxides. All four manganese oxides exhibit different crystal structures. Reference patterns from ICDD are also shown below for matching and comparison.

Table S1. A summary of XRD characteristics for metal oxides

Oxides	Crystal Str.	System	Space group	Lattice Parameters (Å)		PDF number
				a	c	
CoO	Rock salt	Cubic	Fm-3m	4.2500		01-074-2392
Co_3O_4	Spinel	Cubic	Fd-3m	8.1102		01-078-5618
NiO-(i)	Rock salt	Cubic	Fm-3m	4.1771		00-047-1049
$NiCoO_2$	Rock salt	Cubic	Fm-3m	4.2160		00-003-0986
$NiFe_2O_4$	Spinel	Cubic	Fd-3m	8.3344		01-076-6120
Fe_2O_3	Spinel	Cubic	Fd-3m	8.3562		01-078-6916
IrO_2-(i)	Rutile	Tetragonal	P42/mnm	4.5051	3.1586	01-088-0288
RuO_2	Rutile	Tetragonal	P42/mnm	4.4890	3.1049	01-070-2662
$LiCoO_2$	Layered	Rhombohedral*	R-3m	2.8119	14.0334	00-062-0420
$LiNiO_2$	Layered	Rhombohedral*	R-3m	2.8786	14.1984	00-062-0468
$LaCoO_3$	Perovskite	Rhombohedral	R-3m	5.4410	13.0880	00-025-1060
$LaNiO_3$	Perovskite	Rhombohedral	R-3m	5.4570	6.5720	00-033-0711
Mn_2O_3	Scandium oxide type	Cubic	Ia-3	9.4091		00-041-1442
MnO	Rock salt	Cubic	Fm-3m	4.4460		01-075-6876
MnO_2	Rutile	Tetragonal	P42/mnm	4.3983	2.8730	01-071-0071
Mn_3O_4	Spinel	Tetragonal	I41/amd	5.7650	9.4420	01-080-0382

*indexed as hexagonal structure

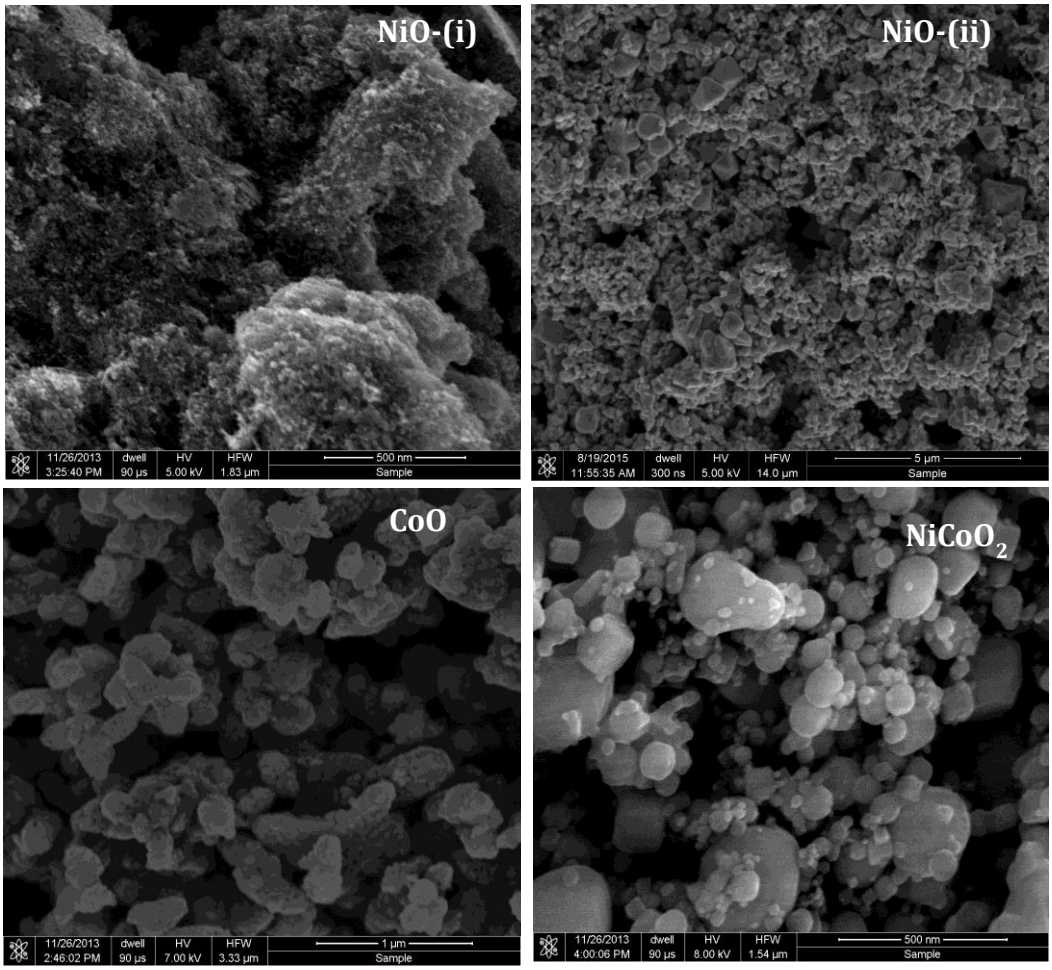

Figure S7. SEM images of immobilized nanoparticles with Nafion onto glassy carbon substrates – rock salt crystal structure based transition metal oxides. Note that NiO-(i) and NiO-(ii) are shown in different scales.

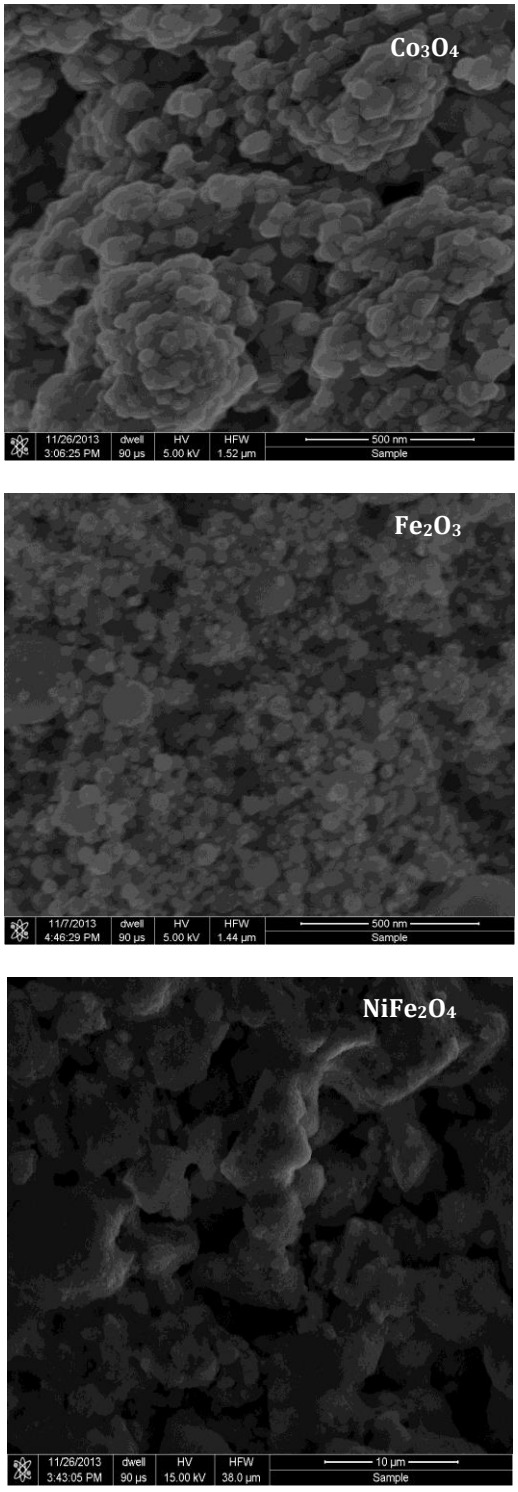

Figure S8. SEM images of immobilized nanoparticles with Nafion onto glassy carbon substrates – spinel crystal structure based transition metal oxides

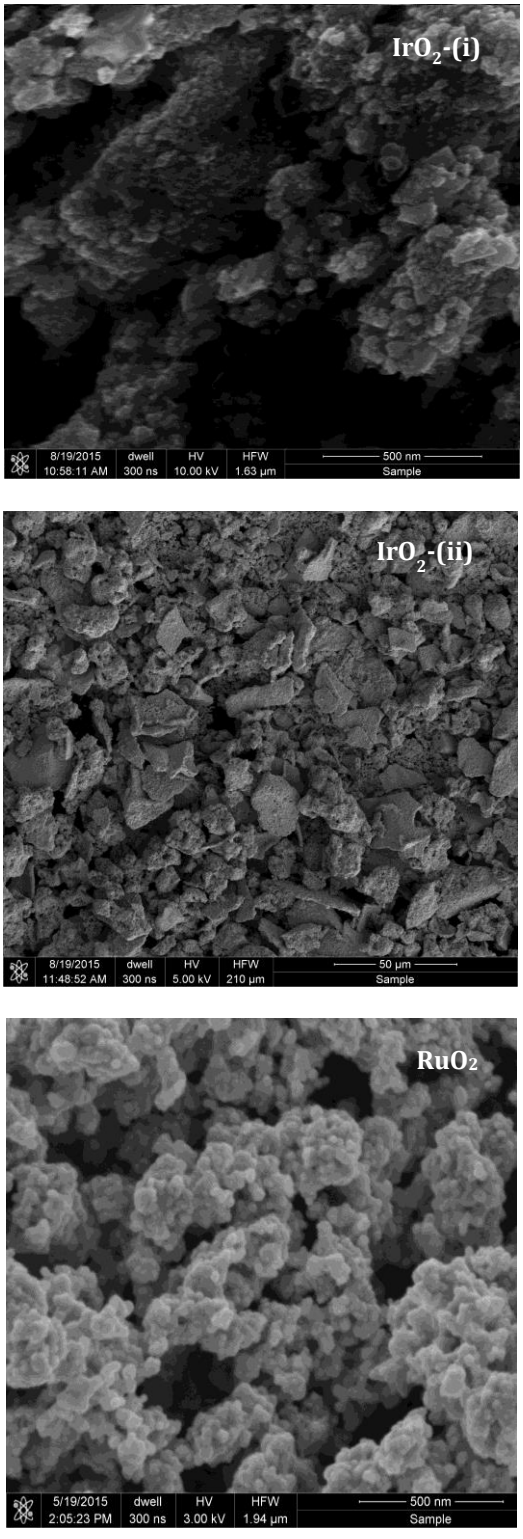

Figure S9. SEM images of immobilized nanoparticles with Nafion onto glassy carbon substrates – rutile crystal structure based noble metal oxides. Note that IrO2-(i) and IrO_2-(ii) are shown in different scales.

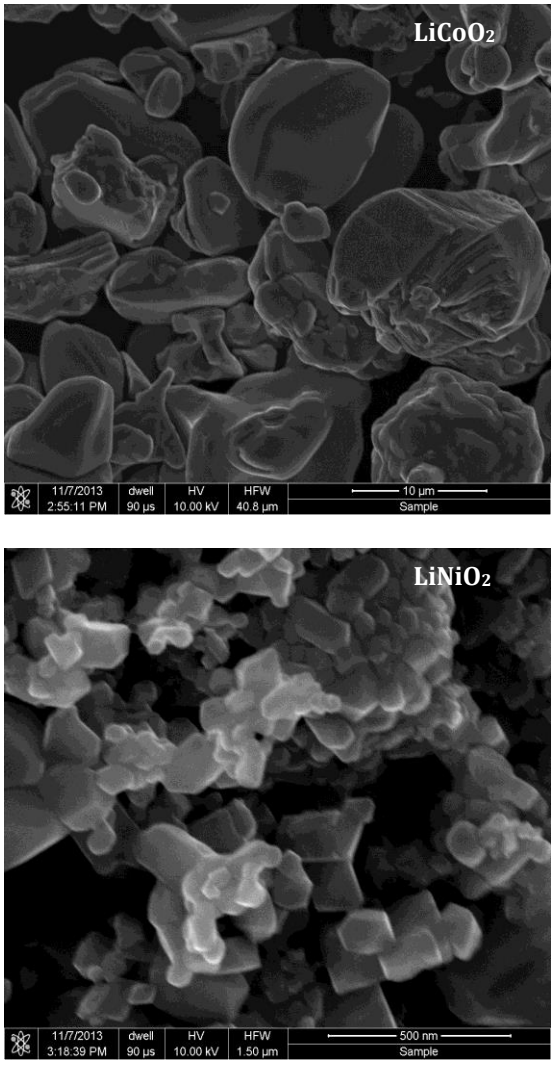

Figure S10. SEM images of immobilized nanoparticles with Nafion onto glassy carbon substrates – layered crystal structure and lithium based metal oxides

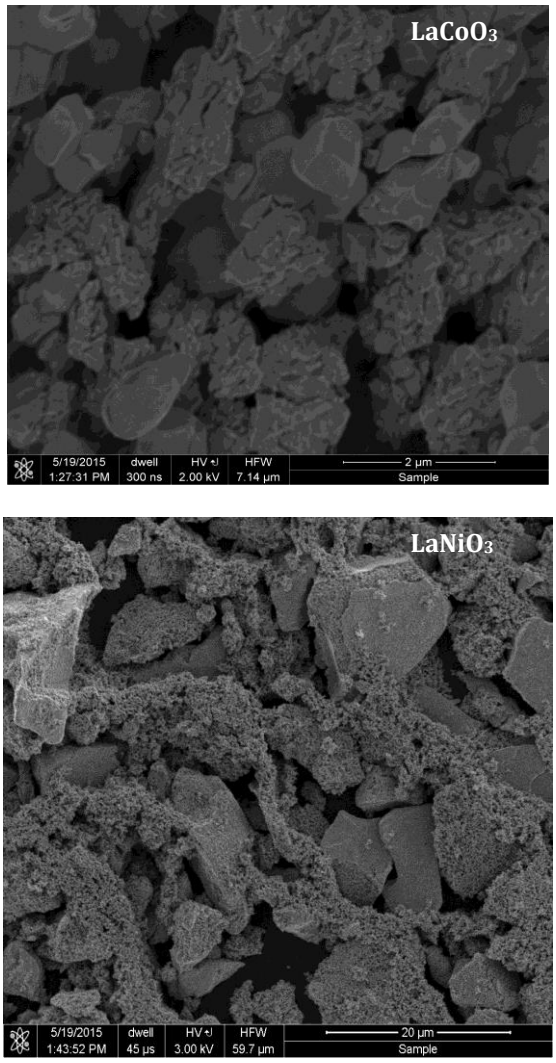

Figure S11. SEM images of immobilized nanoparticles with Nafion onto glassy carbon substrates – perovskite crystal structure and lanthanum based metal oxides

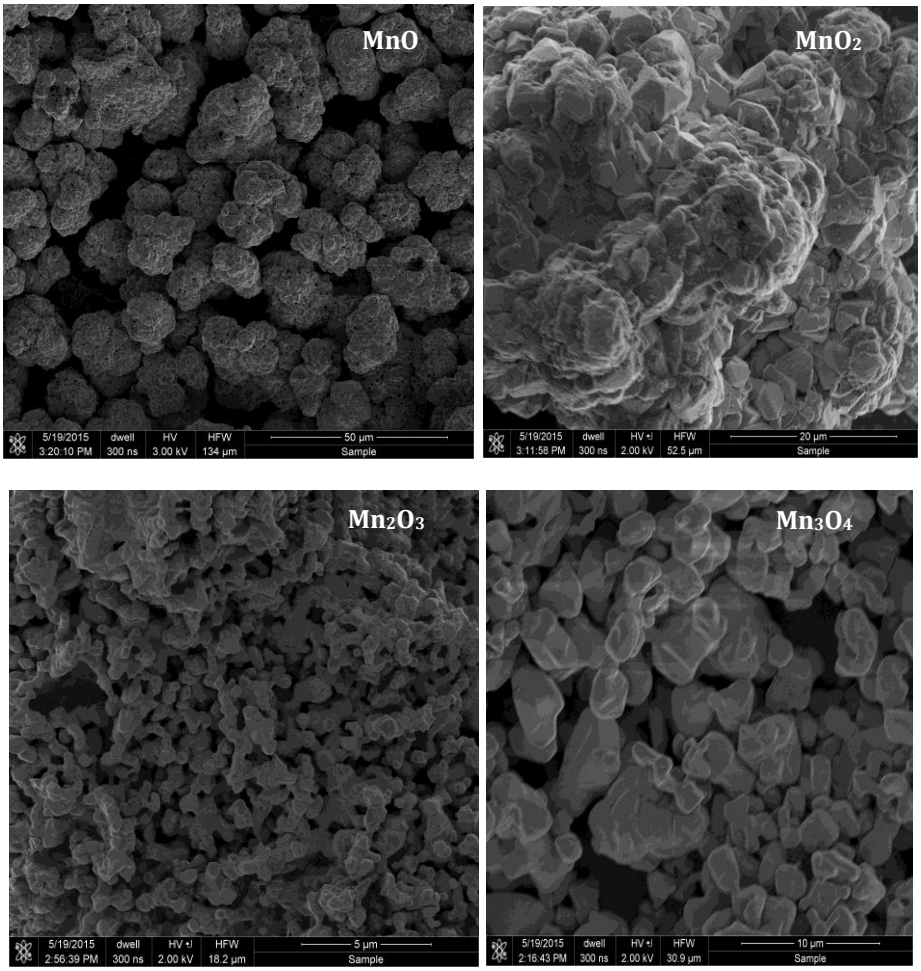

Figure S12. SEM images of immobilized nanoparticles with Nafion onto glassy carbon substrates – various manganese oxides

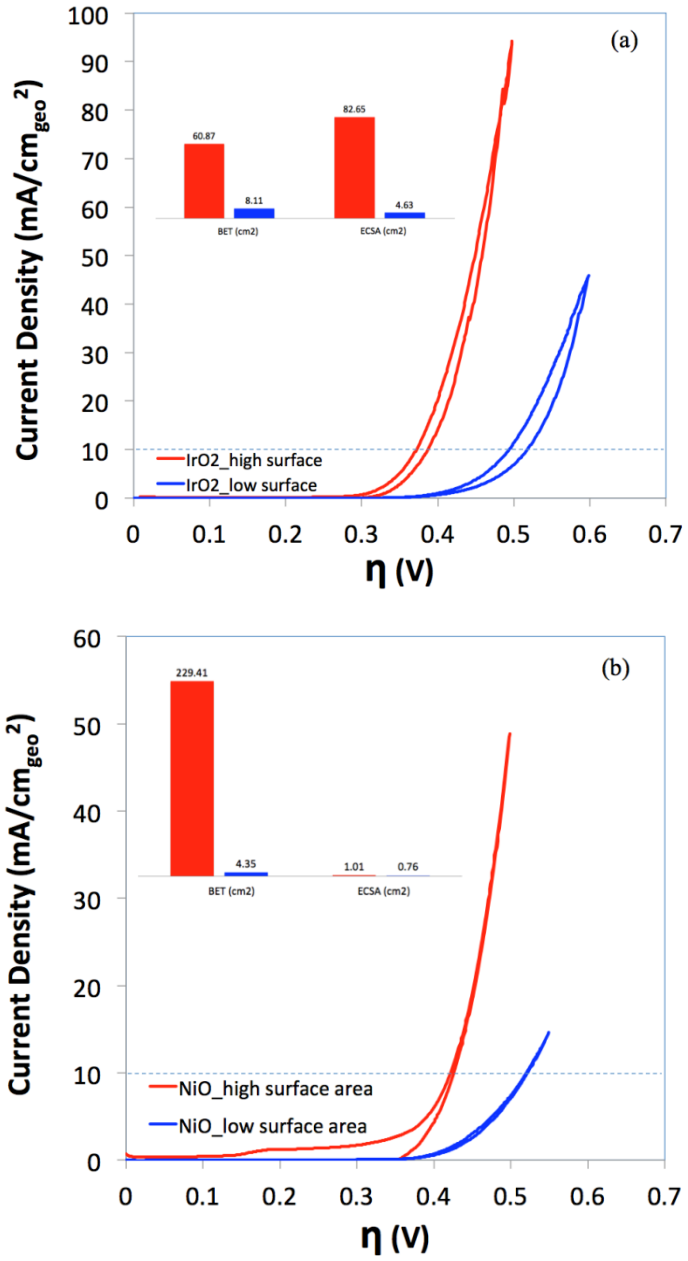

Figure S13. The effect of oxide surface area on OER activity for NiO and IrO_2 particles. The geometric surface area based-rotating disk voltammograms of the oxides with two extreme particle sizes at the same loading (0.8 mg/cm^2) are shown for (a) high surface area IrO_2-(i) (red) and low surface area IrO_2-(ii) (blue), and (b) high surface area NiO-(i) (red) vs. low surface area NiO-(ii) (blue). Surface area by BET and ECSA are shown in insets.

Table S2. Electrical resistivity of metal oxides from literature

Oxides	Sample type	Type of conduction	Resistivity (Ωcm)	Reference
CoO	Single crystal	insulator	10^{9}-10^{10}	[1]
Co_3O_4	Powder	semiconducting	10^{4}	[2, 3]
NiO	Pellet, Powder	semiconducting	10^{-3} - 10^{0}	[4, 5]
$NiCoO_2$	Powder	semiconducting	10^{0}-10^{1}	[4]
$NiFe_2O_4$	Thermal-decomposed film	semiconducting	10^{0}	[6]
Fe_2O_3	Pellet	semiconducting	10^{7}	[7]
IrO_2	Single crystal	metallic	6×10^{-5}	[8]
RuO_2	Single crystal	metallic	$4\text{-}5 \times 10^{-5}$	[8]
$LiCoO_2$	Pellet, single crystal	semiconducting	10^{3}-10^{4}	[9]
$LiNiO_2$	Pellet	semiconducting	10^{0}	[10]
$LaCoO_3$	Pellet	semiconducting	10^{0}-10^{-1}	[11]
$LaNiO_3$	Pellet	metallic	1.22×10^{-3}	[11]
Mn_2O_3	Pellet	semiconducting	5.3-8.0	[12, 13]
MnO	----	insulator	10^{9}-10^{15}	[12, 14]
MnO_2	Single crystal	semiconducting	10^{-1}	[8]
Mn_3O_4	----	semiconducting	10^{6} - 10^{7}	[15]

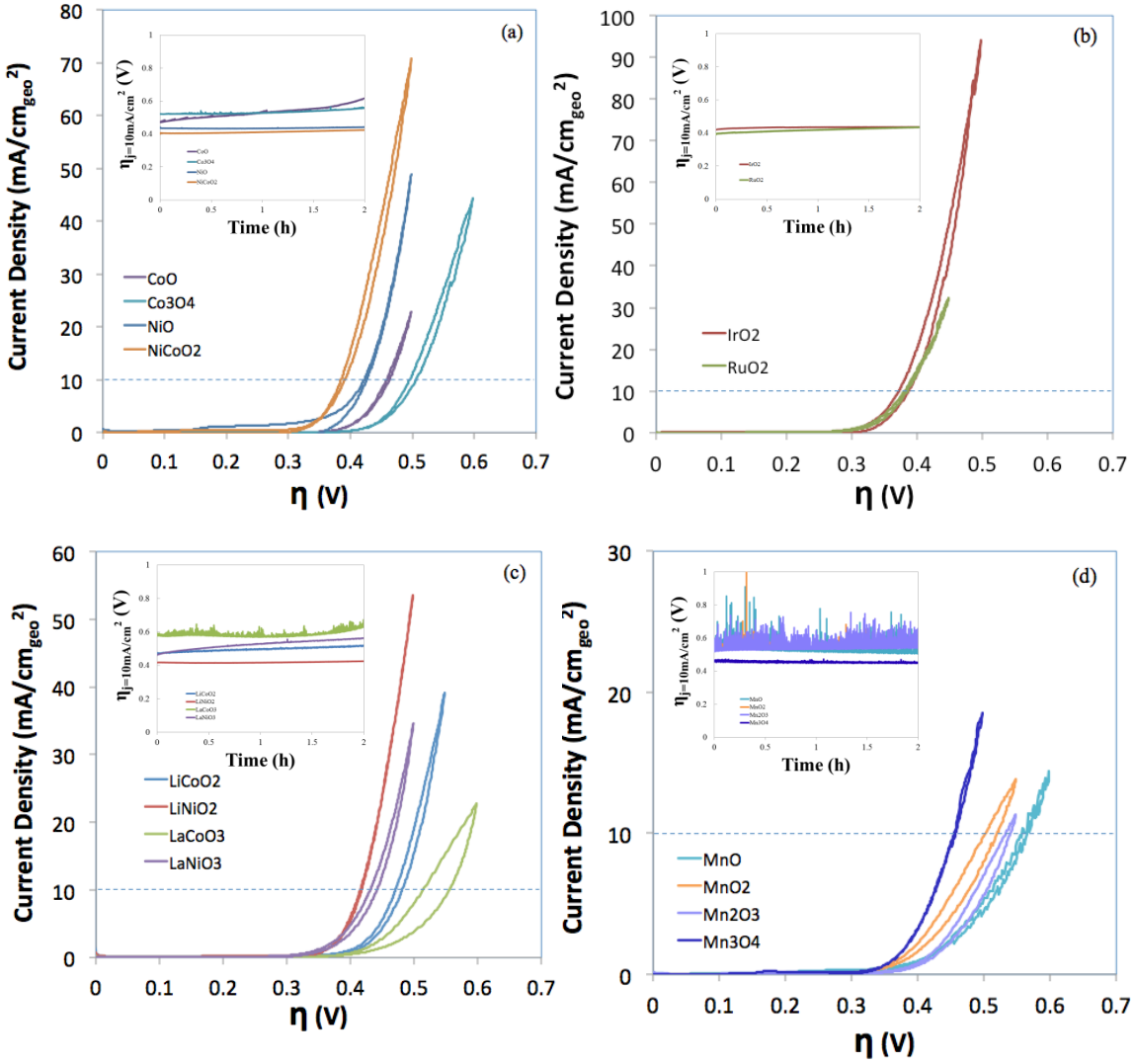

Figure S14. The rotating disk voltammograms of various unsupported metal oxides with the same particle loading in 1M NaOH, 1600 rpm of RDE, 10 mV/s of scan rate. Controlled particle loading = 0.82 mg/cm^2, Estimated Nafion thickness = 0.2 μm. (a) First-row transition metal oxides CoO, Co_3O_4, NiO-(i), and $NiCoO_2$, (b) rutile oxides IrO_2-(i) and RuO_2, (c) layered and perovskite oxides $LiCoO_2$, $LiNiO_2$, $LaCoO_3$, and $LaNiO_3$, and (d) various oxidation states of manganese oxides MnO, MnO_2, Mn_2O_3, and Mn_3O_4. Insets are also shown for 2h-stability of each oxide. The noise in some of the stability measurements is likely due to bubble formation on the electrode surface.

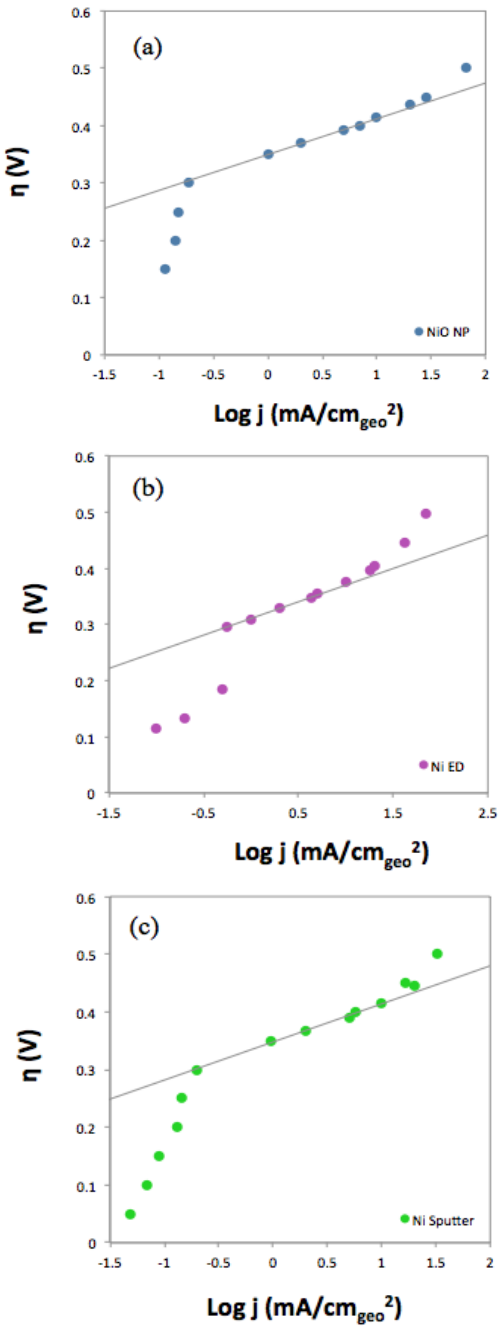

Figure S15. Representative Tafel plots of nickel anodes prepared by various deposition methods (a) drop-casted NiO-(i) nanoparticle, (b) electrodeposited nickel film and (c) sputtered nickel film

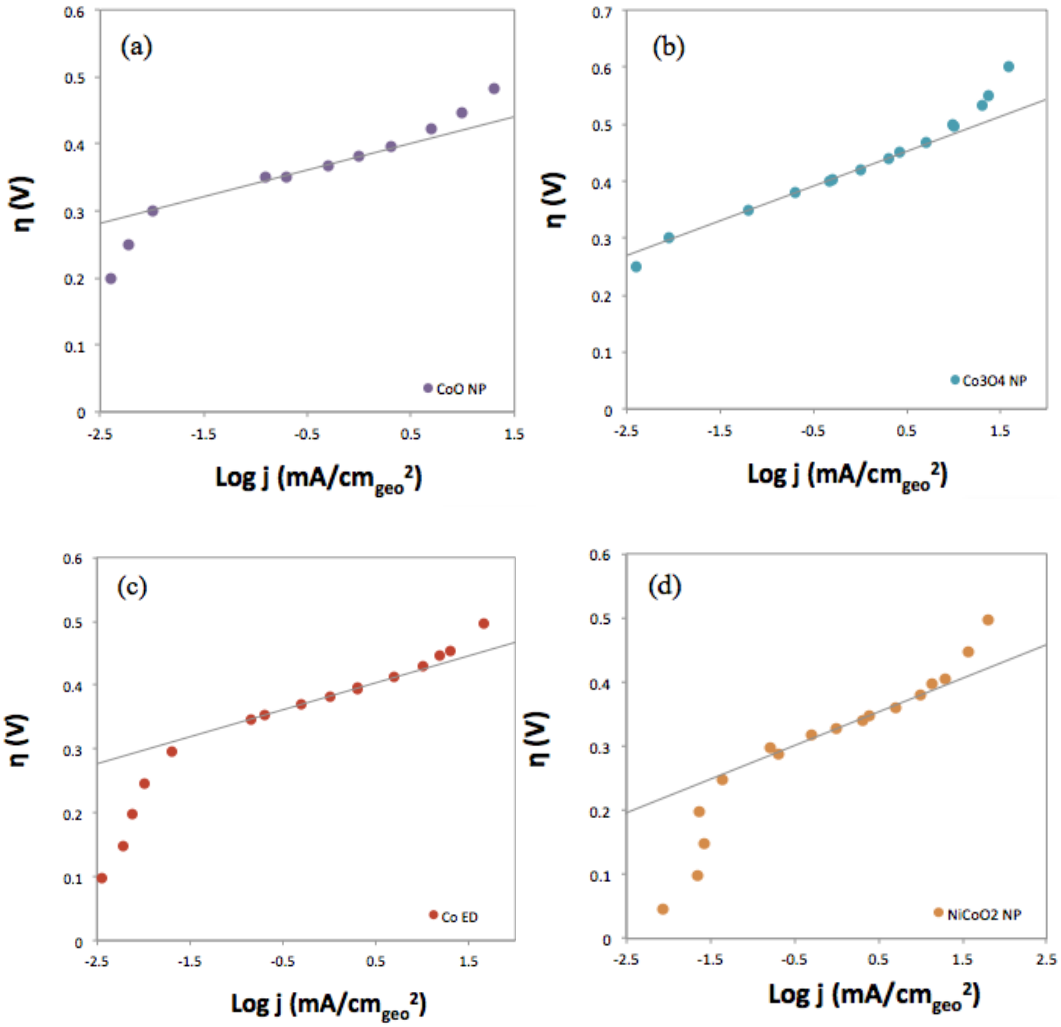

Figure S16. Representative Tafel plots of cobalt based metal oxides (a) drop-casted CoO nanoparticle (b) drop-casted Co_3O_4 nanoparticle (c) electrodeposited Co film, and (d) drop-casted $NiCoO_2$ nanoparticle

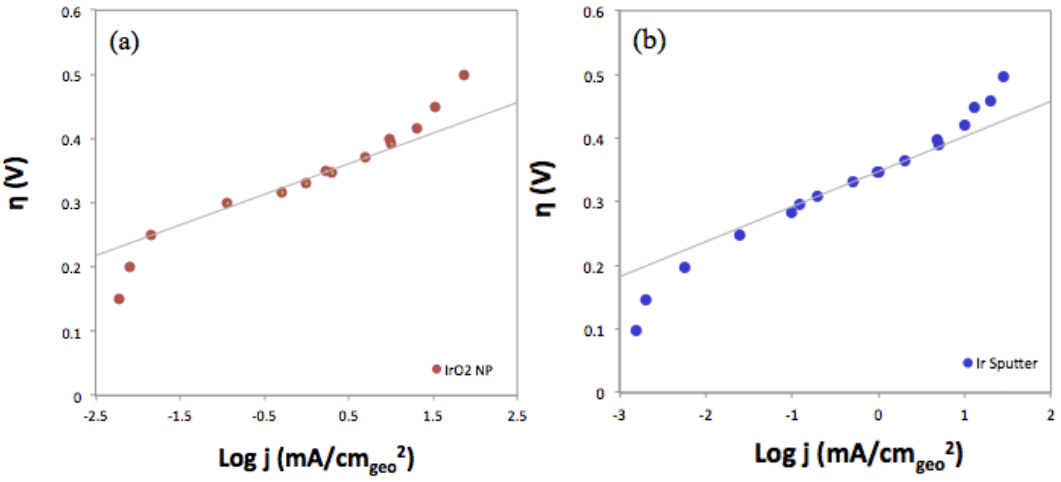

Figure S17. Representative Tafel plots of iridium anodes (a) drop-casted IrO_2-(i) nanoparticle and (b) sputtered Ir film.

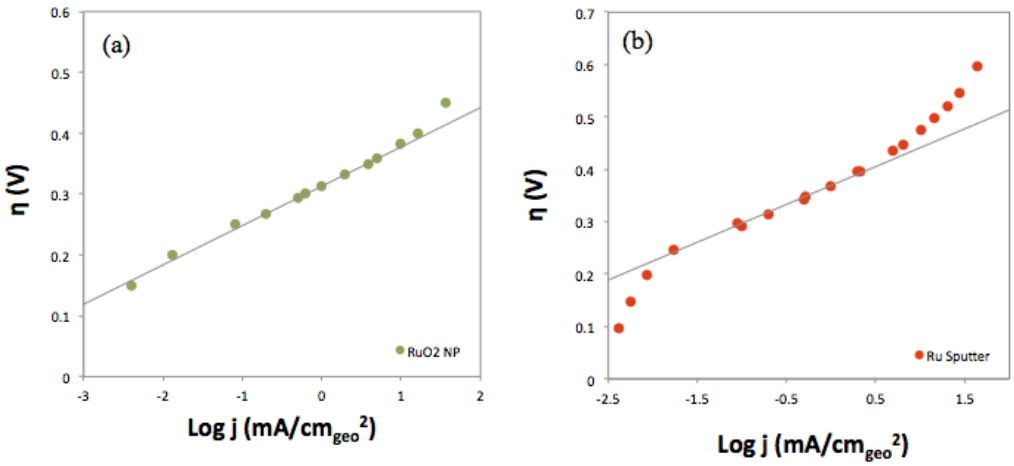

Figure S18. Representative Tafel plots of ruthenium anodes (a) drop-casted RuO_2 nanoparticles and (b) sputtered Ru film.

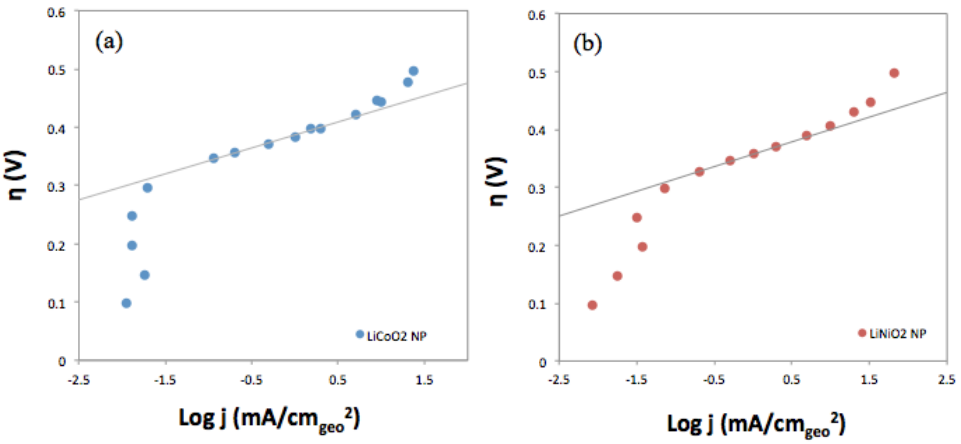

Figure S19. Representative Tafel plots of Lithium based layered oxides (a) drop-casted $LiCoO_2$ particle and (b) drop-casted $LiNiO_2$ particle

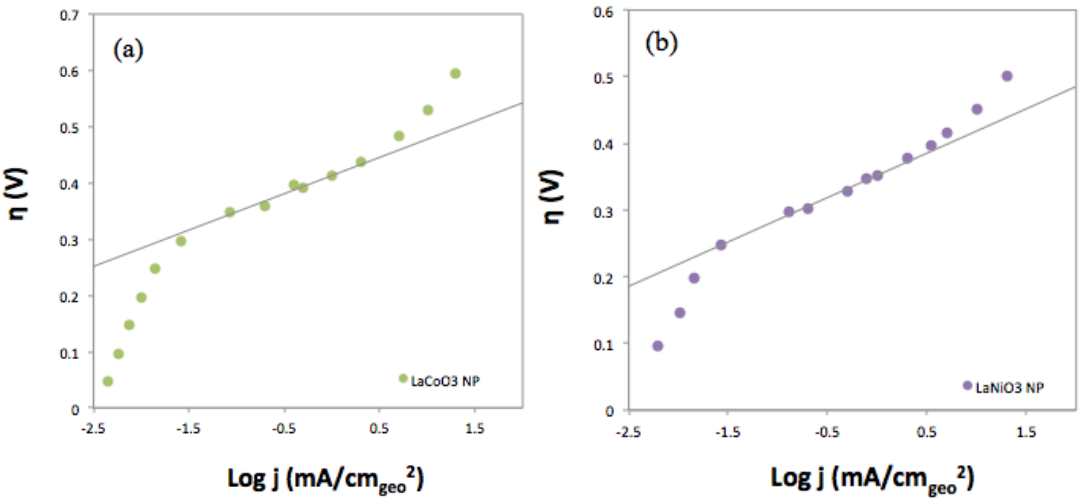

Figure S20. Representative Tafel plots of Lanthanum based perovskite oxides (a) drop-casted $LaCoO_3$ particle and (b) drop-casted $LaNiO_3$ particle.

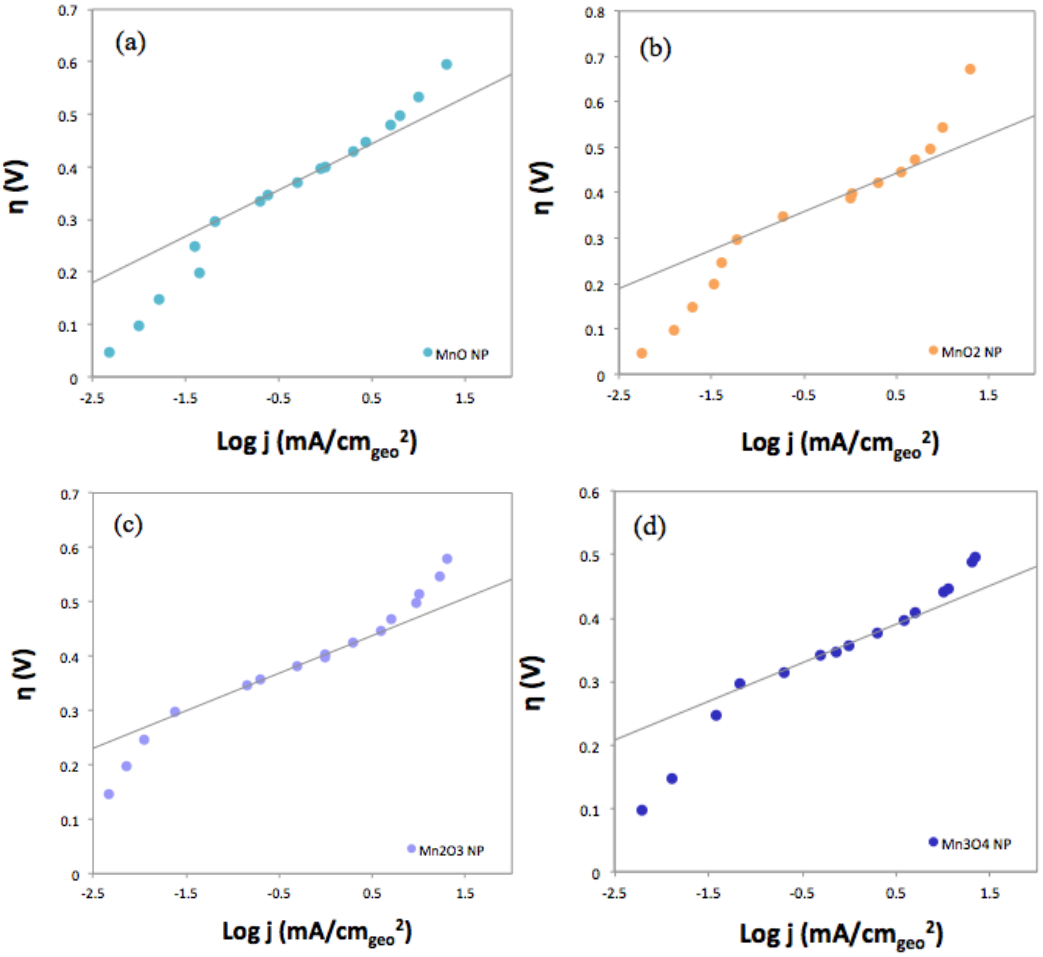

Figure S21. Representative Tafel plots of various manganese oxide particles (a) drop-casted MnO, (b) drop-casted MnO_2, (c) drop-casted Mn_2O_3 and (d) drop-casted Mn_3O_4.

Comparisons of OER Activity for Particulate Films and Other Deposited Films

For select systems the activity of the nanoparticle film was directly compared to those for previously-studied thin film catalysts prepared by other deposition methods such as sputtering and electrodeposition. RDEVs of five different oxide particles (IrO_2, NiO, RuO_2, CoO, and Co_3O_4) were directly compared to deposited thin-films with similar qualitative composition, as shown in Fig. S22. In the case of IrO_2 and NiO, the catalytic activity of the drop-casted particulate catalysts closely matched those of the other deposited films. In the case of RuO_2, CoO, and Co_3O_4, there was a larger discrepancy in the activity of the drop-casted particles and related deposited films. Note that this discrepancy may be partially due to differences in surface area and loading between the materials, and that in each case the catalysts operated overpotentials at 10 mA/cm_{geo}^2 varying by no more than ~0.12 V. Moreover, as shown in Fig. S23, the Tafel slopes of the nanoparticulate catalysts and their corresponding deposited films are very similar with the exception of Co_3O_4, implying that the basic catalytic mechanisms are largely unchanged regardless of deposition method. The difference in the Tafel slope between the Co_3O_4 nanoparticulate system and the two other Co-based systems (CoO nanoparticle and electrodeposited Co) in Fig. S23 (d) may suggest that the oxidation state of the electrodeposited Co system more resembles that of CoO and not Co_3O_4 during OER catalysis.

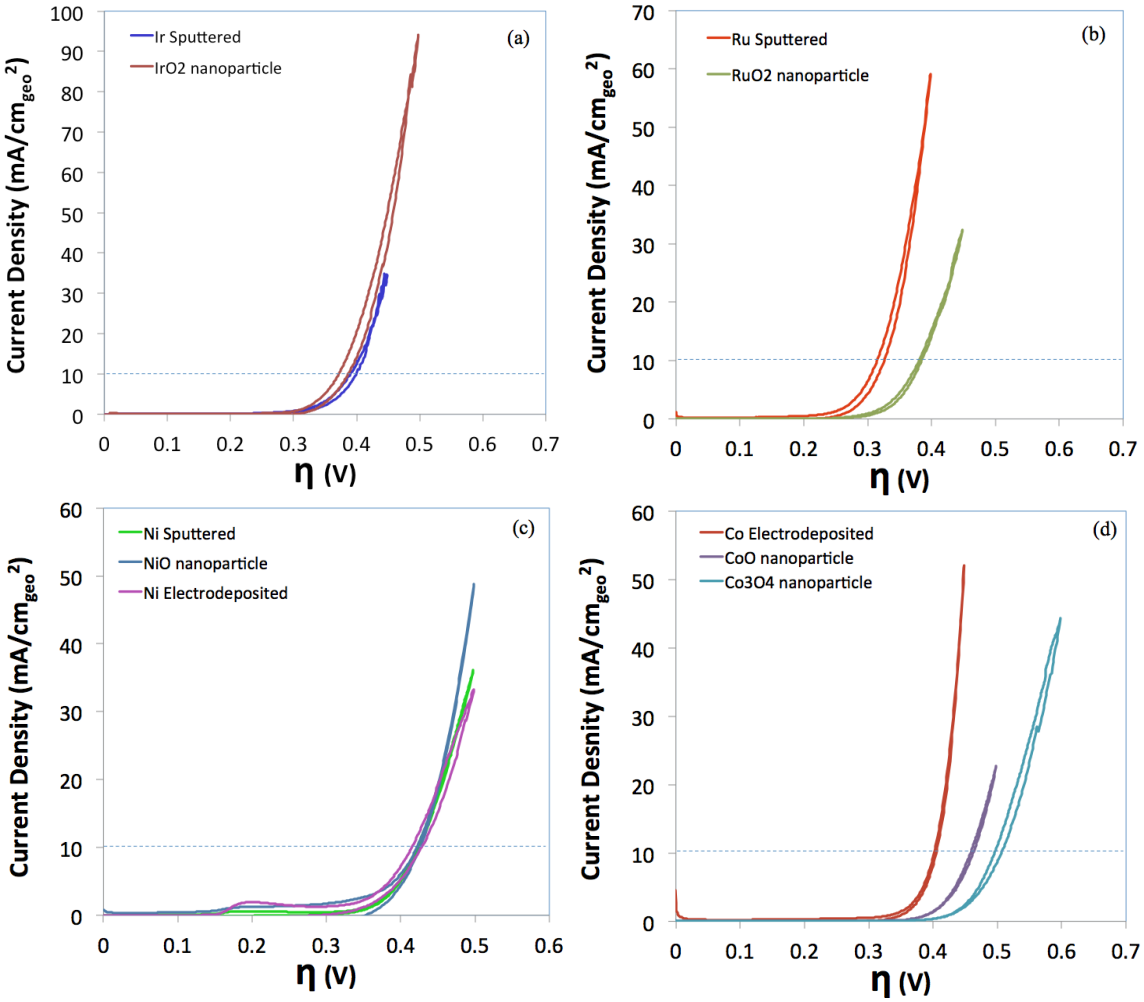

Figure S22. The comparison of OER activity between drop-casted oxide nanoparticles and thin films synthesized by other preparation methods. Representative rotating disk voltammograms of the OER were obtained at 10 mV/s scan rate and 1600 rpm in 1M NaOH. The horizontal dashed line at 10 mA/cm$_{geo}^2$ per geometric area is the current density expected for a 10% efficient solar water-splitting device. (a) comparison of immobilized IrO_2-(i) nanoparticle and sputtered Ir (b) comparison of immobilized RuO_2 nanoparticle and sputtered Ru (c) comparison of immobilized NiO-(i) nanoparticle, sputtered Ni, and electrodeposited Ni and (d) comparison of immobilized CoO nanoparticle, immobilized Co_3O_4 nanoparticle, and electrodeposited Co.

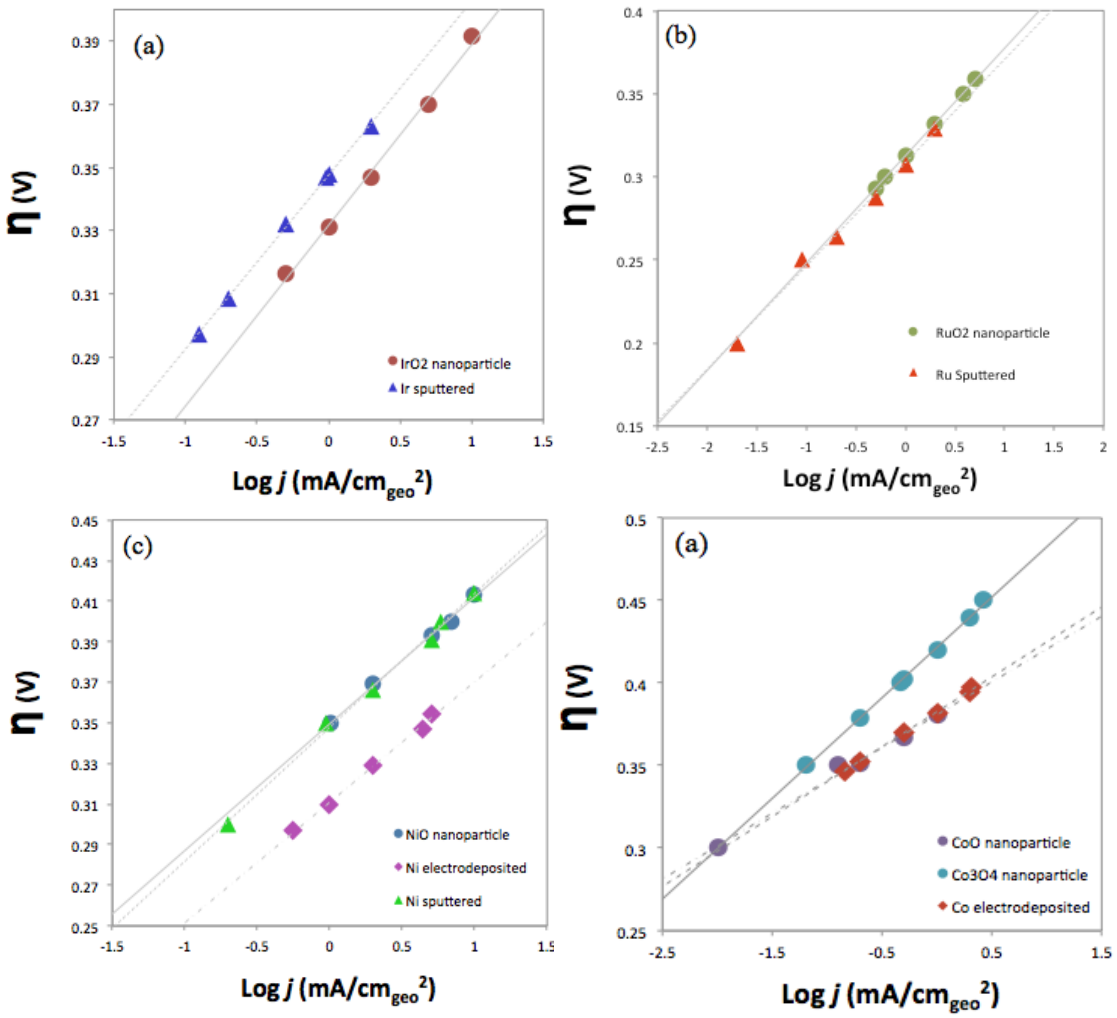

Figure S23. The comparison of Tafel slopes for (a) immobilized IrO_2-(i) nanoparticle (47.7 mV/dec) and sputtered Ir film (55.1 mV/dec) (b) immobilized RuO_2 nanoparticle (64.6 mV/dec) and sputtered Ru film (62.2 mV/dec) (c) immobilized NiO-(i) nanoparticle (62.4 mV/dec), sputtered Ni film (66.0 mV/dec), and electrodeposited Ni film (59.3 mV/dec) and (d) immobilized CoO nanoparticle (39.8 mV/dec), immobilized Co_3O_4 nanoparticle (60.9 mV/dec) and electrodeposited Co film (42.3 mV/dec). The plots were obtained from steady state conditions of RDE (30 s potentiometric steps and amperometric steps) at 1600 rpm in 1M NaOH. Raw data plots are shown in Fig. S15 – S18.

Reference

1. G. M. Joshi, M. Pai, H. R. Harrison, C. J. Sandberg, R. Aragón and J. M. Honig, *Materials Research Bulletin*, 1980, **15**, 1575-1579.
2. C. Iwakura, A. Honji and H. Tamura, *Electrochimica Acta*, 1981, **26**, 1319-1326.
3. P. Rasiyah and A. C. C. Tseung, *Journal of The Electrochemical Society*, 1983, **130**, 365-368.
4. S. M. Jasem and A. C. C. Tseung, *Journal of The Electrochemical Society*, 1979, **126**, 1353-1360.
5. S. Koide, *Journal of the Physical Society of Japan*, 1965, **20**, 123-132.
6. C. Iwakura, M. Nishioka and H. Tamura, *NIPPON KAGAKU KAISHI*, 1982, **1982**, 1136-1140.
7. Y. Y. Shimpei Ito, and Jin Mizuguchi, *Materials Transactions* 2010, **51**.
8. D. B. Rogers, R. D. Shannon, A. W. Sleight and J. L. Gillson, *Inorganic Chemistry*, 1969, **8**, 841-849.
9. F. Sauvage, J. M. Tarascon and E. Baudrin, *The Journal of Physical Chemistry C*, 2007, **111**, 9624-9630.
10. I. Saadoune and C. Delmas, *Journal of Materials Chemistry*, 1996, **6**, 193-199.
11. J. O. M. Bockris and T. Otagawa, *Journal of The Electrochemical Society*, 1984, **131**, 290-302.
12. J. B. Goodenough, *Progress in Solid State Chemistry*, 1971, **5**, 145-399.
13. M. Morita, C. Iwakura and H. Tamura, *Electrochimica Acta*, 1979, **24**, 357-362.
14. V. G. Bhide and R. H. Dani, *Physica*, 1961, **27**, 821-826.
15. R. Waser, in *Keramik*, ed. H. Schaumburg, Vieweg+Teubner Verlag, 1994, DOI: 10.1007/978-3-663-05976-9_4, ch. 4, pp. 129-218.